analytical chemistry

pubs.acs.org/ac Article

Three-Dimensional Mass Spectrometric Imaging of Biological Structures Using a Vacuum-Compatible Microfluidic Device

Wenxiao Guo, Michal Kanski, Wen Liu, Mikołaj Gołuński, Yadong Zhou, Yining Wang, Cuixia Cheng, Yingge Du, Zbigniew Postawa,* Wei David Wei,* and Zihua Zhu*

Cite This: *Anal. Chem.* 2020, 92, 13785−13793 Read Online

ACCESS | Metrics & More | Article Recommendations | Supporting Information

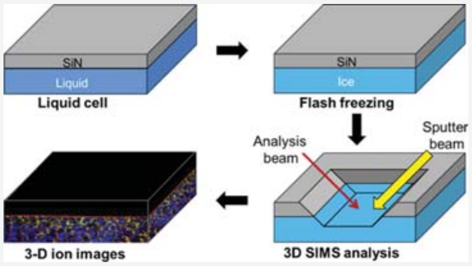

ABSTRACT: Three-dimensional (3D) molecular imaging of biological structures is important for a wide range of research. In recent decades, secondary-ion mass spectrometry (SIMS) has been recognized as a powerful technique for both two-dimensional and 3D molecular imaging. Sample fixations (e.g., chemical fixation and cryogenic fixation methods) are necessary to adapt biological samples to the vacuum condition in the SIMS chamber, which has been demonstrated to be nontrivial and less controllable, thus limiting the wider application of SIMS on 3D molecular analysis of biological samples. Our group recently developed *in situ* liquid SIMS that offers great opportunities for the molecular study of various liquids and liquid interfaces. In this work, we demonstrate that a further development of the vacuum-compatible microfluidic device used in *in situ* liquid SIMS provides a convenient freeze-fixation of biological samples and leads to more controllable and convenient 3D molecular imaging. The special design of this new vacuum-compatible liquid chamber allows an easy determination of sputter rates of ice, which is critical for calibrating the depth scale of frozen biological samples. Sputter yield of a 20 keV Ar_{1800}^+ ion on ice has been determined as 1500 (±8%) water molecules per Ar_{1800}^+ ion, consistent with our results from molecular dynamics simulations. Moreover, using the information of ice sputter yield, we successfully conduct 3D molecular imaging of frozen homogenized milk and observe network structures of interesting organic and inorganic species. Taken together, our results will significantly benefit various research fields relying on 3D molecular imaging of biological structures.

Three-dimensional (3D) mass spectrometric analysis of biological samples provides important molecular information for understanding the composition and behavior of different biological structures, making it critical for research in fields ranging from environmental to biomedical science.[1−7] Secondary-ion mass spectrometry (SIMS) has been recognized as a promising technique for label-free 3D molecular analysis of biological samples.[8−14] SIMS detects the secondary ions sputtered from a sample surface by a primary ion beam and maps the lateral distribution of chemical species on the outermost layer of the sample with submicron lateral resolution.[12] Recent developments have demonstrated that by using high-flux polyatomic clusters as the primary ion beam, the top layer of samples can be removed with nanometer precision.[15−21] Hence, 3D imaging of biological samples can be constructed by alternately switching the instrument between sputtering mode and analysis mode, and stacking two-dimensional molecular images obtained at different depth in the analysis mode.[8,14]

However, a wider application of SIMS in 3D molecular analysis is limited by its special requirements for sample preparation. Sample fixation for SIMS analysis is necessary as the instrument is operated under a high-vacuum environment. Cryogenic fixation is most commonly used because it maintains the integrity of biological samples.[22−25] Freeze-drying is a representative cryogenic fixing strategy in which a sample is rapidly frozen, slowly dried under vacuum by allowing the ice sublimation, and analyzed under room temperature.[10,26−28] Using this preparation method, Gilmore and co-workers obtained 3D metabolic imaging of cells treated with amiodarone on the subcellular level using OrbiSIMS, successfully unraveling the mechanism behind the drug-induced phospholipidosis that had long been under debate.[10] However, despite its wide application, freeze-drying preparation was reported to cause occasional migration of cellular components and the surface contamination of samples.[25,27,29−31] Alternatively, samples can be prepared via freeze-fracturing, in which a liquid sample is rapidly frozen and fractured from the middle to expose the samples in a frozen-hydrated status.[32−37] Fletcher and co-workers demonstrated the compatibility of freeze-fracturing with 3D SIMS by mapping the cellular components of HeLa cells.[37] However,

Received: May 22, 2020
Accepted: September 2, 2020
Published: September 2, 2020

ACS Publications

https://dx.doi.org/10.1021/acs.analchem.0c02204

although the freeze-fracturing strategy retains original cellular structures of samples and generates frozen-hydrated samples that exhibit higher yield of secondary ions,[38−40] it has the shortcomings such as sophisticated operations and non-reproducible generation of fracture planes.[25] As a result, a more convenient and reproducible sample preparation strategy is needed to make 3D molecular analysis based on SIMS more adaptable to various biological samples.

In situ liquid SIMS, recently developed by our group, sheds light on overcoming these limitations in sample preparation. In a typical design of *in situ* liquid SIMS, a traditional time-of-flight (TOF) SIMS instrument is equipped with a vacuum-compatible microfluidic device.[41−49] The liquid chamber of a microfluidic device has well-controlled dimensions and is tightly sealed under a thin silicon nitride (SiN) membrane. A redesign of vacuum-compatible microfluidic device makes flash-freezing of the whole device possible, enabling the preparation of frozen-hydrated samples with precisely confined shapes and total volume. Similarly, 3D molecular imaging on these frozen samples can also be obtained by conducting multiple sputtering-analysis cycles.

In this contribution, we demonstrated the potential of a newly designed vacuum-compatible microfluidic device in conducting 3D molecular imaging of biological structures with submicron resolution. Imaging of 3D networks of homogenized milk was conducted as a proof-of-concept. Meanwhile, it is noteworthy that to gain an accurate depth profile using SIMS, knowledge of sputter rate of samples is necessary for *z*-correction.[50−53] The sputter rate of ice is of particular interest because the major component in most biological samples is water (i.e., ice in the frozen state). Previous studies achieved this by coupling SIMS with a low-temperature quartz crystal microbalance (QCM) to determine the amount of samples removed in each cycle of sputtering.[19,51] Herein, we showed that the sputter rate can be more readily obtained for ice using the innovation in this work. The liquid cell with precisely controlled volume determined the total amount of sample molecules, which, combined with the time required to completely remove samples via sputtering, allowed the estimation of the sputter rate. For the first time, the sputter rate of ice for a 20 keV Ar cluster primary ion was experimentally determined. Molecular dynamics (MD) simulations of the sputtering process further confirmed the accuracy of the sputter rate measurement. Taken together, we demonstrated the newly developed strategy as a convenient and controllable method for 3D molecular imaging of various samples. The successful development of this method would offer great opportunities to gain a more comprehensive understanding of compositions and behaviors of a wide range of biological samples that are crucial to human, industry, and environmental applications.

■ EXPERIMENTAL SECTION

Fabrication of the Microfluidic Device. We redesigned a high vacuum-compatible microfluidic device based on our previously reported method with some extensive adaptations.[43,46] In brief, as shown in Figure 1a, a silicon frame [5.0 mm (L) × 5.0 mm (W) × 0.2 mm (H)] with a thin SiN membrane (100 nm in thickness, window size 0.5 mm × 0.5 mm) immobilized under it was sealed on the top of a liquid chamber that was previously sculptured with a size of 3.0 mm (L) × 3.0 mm (W) × 0.05 mm (H) on a copper (Cu) block. Copper block's size was 10.0 mm (L) × 12.0 mm (W) × 2.0 mm (H). Compared to our previous design, the thickness of the device was greatly reduced for better thermal transfer. After introducing a liquid sample of interest through two liquid channels, ends of two liquid channels were sealed, and then the microfluidic device was quickly put into ethylene precooled in liquid nitrogen for a flash-freezing. After freezing, the frozen sample was quickly transferred onto a temperature-controllable sample holder (purchased from IONTOF) precooled to −110 °C in the intro-chamber. The transfer of sample was protected in a glovebag under N_2 flow to minimize possible ice condensation on the sample surface. After pumping down the intro-chamber, the sample holder loaded with the microfluidic device was transferred into the main chamber for 3D SIMS imaging analysis. The temperature of the sample was controlled at −110 °C during the SIMS testing.

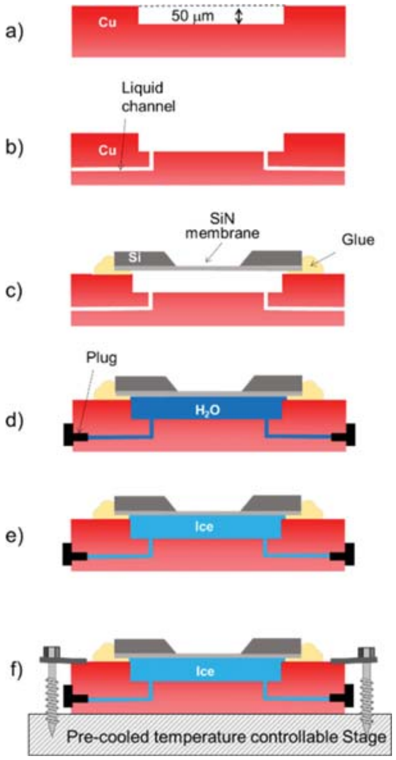

Figure 1. Schematic showing the design of a vacuum-compatible device for 3D molecular imaging of frozen samples using ToF-SIMS. (a) Liquid chamber with ca. 50 μm depth was prepared on a Cu block. (b) Two liquid channels were prepared, through which liquids can enter and leave the liquid chamber. (c) Thin SiN membrane immobilized beneath a Si frame was glued onto the liquid chamber. (d) Liquid samples can be introduced into the liquid chamber through liquid channels, and the two channels can be sealed with plugs, making the whole device vacuum compatible. (e) Device filled with liquid was flash-frozen. (f) Frozen device was quickly immobilized onto a precooled temperature-controllable sample holder for SIMS measurement. Photos of the actual device and sample holder are seen in Figure S1.

It has been reported that for a thin aqueous sample (e.g., less than 10 μm), the cooling rate can be very fast, and water can become vitrified ice with little volume expansion.[54] In this work, the cooling rate might not be fast enough, and some volume expansion was expected. To address this issue, we set the liquid chamber to ca. 0.05 mm (50 μm) in depth. Such a shallow depth would only lead to at most 5 μm expansion in thickness during the water-to-ice transition, and results showed that the device could withstand it without any damage. Meanwhile, reasonably reproducible SIMS depth profiling measurement was obtained.

3D SIMS Measurements. We performed SIMS measurements using a ToF-SIMS 5 instrument (ION-TOF GmbH, Münster, Germany). Dual-beam noninterlaced depth profiling mode was used. A 20.0 keV Ar cluster ($Ar_{1800\pm400}^+$) ion beam was used as the sputtering beam, and a 25 keV Bi_3^+ beam was used as the analysis beam for signal collection. The Ar cluster sputtering beam (20−30 μm in diameter, 14.2 ± 0.1 nA) was scanned over a 300 × 300 μm^2 area. To measure the sputter rate of ice, ice over 50 μm in thickness would be sputtered away; therefore, beam alignment would be a problem because the incident angle of both Ar cluster beam and the Bi_3^+ beam was 45°. To ensure that the Cu signals from the bottom of the liquid chamber could be obtained, the 25 keV Bi_3^+ beam was scanned over a 400 × 400 μm^2 area, larger than the Ar cluster sputter crater. For the testing of ice sputter rate, the 25 keV Bi_3^+ analysis beam was operated in the high-mass resolution mode by focusing the size of beam to 5 μm in diameter. The depth profiling measurement was stopped once clear Cu signals were observed. A low-energy (10 eV) electron flood gun was used for charge compensation in all measurements. During data reconstruction, only the Cu signal area was selected.

Dual-beam noninterlaced depth profiling mode was then used in the 3D imaging of frozen milk samples. The setting of Ar cluster ion-sputtering beam was the same as that used for the sputtering of ice. However, in this scenario, in order to collect high-quality imaging data, the 25 keV Bi_3^+ analysis beam was operated in high-spatial resolution mode by focusing the size of beam to ca. 400 nm in diameter, and the width of a Bi_3^+ pulse was about 150 ns with a pulse current of 0.36 ± 0.01 pA at a 10 kHz repeating frequency. This beam setting has been regularly used for *in situ* SIMS analysis,[46−49] and more details of adjustment can be seen in our previous paper.[55] During imaging data collection, the 25 keV Bi_3^+ beam was scanned over a 100 × 100 μm^2 area with 256 × 256 pixels at the center of the Ar cluster sputter crater. It should be noted that the signal intensity significantly decreased after the removal of ca. 20 μm of material possibly because of misalignment of the Bi_3^+ ion beam and the Ar cluster ion beam. Therefore, a 400 × 400 μm^2 Bi_3^+ analysis area was used in the measurement of ice sputter rate.

It should be noted that we used a Faraday cup built in an IONTOF sample holder to measure the Ar cluster ion beam current and the pulsed Bi_3^+ beam current. The IONTOF sample holder was grounded during SIMS testing, making the current measurement results highly stable and accurate.

MD Simulations. MD simulations have been used to model the impact of Ar cluster and C_{60} projectiles on ice samples. In this approach, the movement of particles is determined by integrating Hamilton's equations of motion. A detailed description of the MD method can be found elsewhere.[56] Forces between argon atoms are described by the Lennard-Jones potential[57] splined with KrC potential[58] for an accurate description of high energy collisions. The ReaxFF force field trained for modeling water systems is used to describe interactions between hydrogen, carbon, and oxygen atoms.[59] Finally, the interaction between argon and hydrogen and oxygen atoms is described by repulsive ZBL potential.[60] Electronic energy losses are ignored because of a low velocity of moving projectile atoms. The shape and size of the samples are chosen based on visual observations of energy transfer pathways stimulated by projectile impacts. As a result, for Ar_{1800} and C_{60} impacts, a sample shape of a spherical dome with a diameter of 60 nm and height of 20 nm and a half sphere with a diameter of 40 nm are used, respectively. Rigid and stochastic regions are applied to simulate the thermal bath that keeps the sample at the required temperature of 0 K, which prevents the reflection of pressure waves generated by cluster projectile impacts from the boundaries of the system and maintains the shape of the sample.[56,61] Samples consist of water molecules arranged in an amorphic ice structure. Projectiles are given an initial kinetic energy of 20 keV with an incident angle of 45°. Simulations extend up to 50−70 ps depending on the sample. This value is large enough to achieve the saturation in the ejection yield versus time dependence. The simulations are performed with LAMMPS software package.[62]

RESULTS AND DISCUSSION

Determination of Ice Sputter Yield. In the past decade, the Ar cluster ion beam has been widely used for 3D imaging of frozen biological samples whose major component is ice (i.e., water under normal condition).[28,63,64] Hence, the sputter yield of ice using an Ar cluster primary ion is needed to accurately construct 3D molecular imaging and has not been experimentally determined yet. Therefore, the sputter yield of ice was first determined in this work. Figure 2 shows a set of typical depth profiling data of an ice sample, which illustrates that the Ar cluster beam sputtered through the SiN membrane in about 80 s while another 1340 s was needed for the beam to sputter through the ice layer, yielding Cu signals from the bottom of device. To determine the accurate sputter yield, the thickness of the ice also needs to be carefully determined. Although the depth of the liquid chamber was about 50 μm, as shown in Figure 1a, glue was used to immobilize the SiN membrane-Si frame on top of the liquid chamber, which may generate additional space between the SiN membrane and the Cu block (Figure 1c). Therefore, after SIMS testing, a profilometer was used to measure the distance from the top of the Si frame to the bottom of the liquid chamber (ca. 252 μm), and a scanning electron microscope was used to measure the thickness of the Si frame and SiN membrane (ca. 191 μm), from which the exact thickness of ice in the liquid chamber was

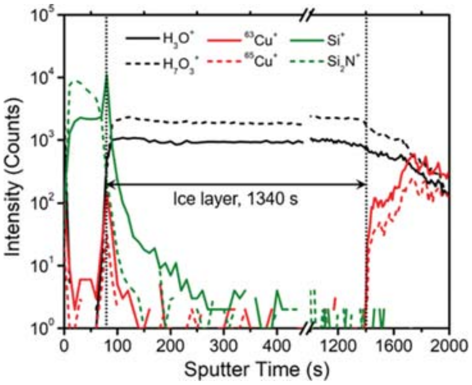

Figure 2. Depth profiles of selected ions during depth profiling of ca. 61 μm of ice. A 14.2 nA 20 keV Ar_{1800}^+ beam was used for sputtering with a scanning area of 300 × 300 μm^2. The data were reconstructed using only Cu^+ area.

estimated as 61 μm (Figure S2, supposing no volume change during flash-freezing). In other words, a 14.2 nA 20 keV Ar_{1800}^+ beam used ca. 1340 s to sputter through an ice layer with a depth of 61 μm and a scanning area of 300 × 300 μm^2.

The sputter yield N (the number of H_2O molecules per Ar cluster ion) was calculated using equation eq 1. Based on the thickness of ice and the data, as shown in Figure 2, the sputter yield of ice using Ar cluster ion can be calculated (details of calculation are found in the Supporting Information). Multi-measurements were performed (more details are seen in the Supporting Information), and the sputter yield of ice was determined as 1500 (±8%) H_2O molecules per 20 keV Ar_{1800}^+ ion.

$$N = \frac{N_{\text{ice}}}{N_{\text{ion}}} \tag{1}$$

Cryo-QCM was utilized to measure sputter yields of ice using 20 keV Au_3^+ and C_{60}^+ primary ions, showing that ice sputter yields were about 1000−1200 H_2O molecules for a 20 keV Au_3^+ ion and about 1800−2500 H_2O molecules for a 20 keV C_{60}^+ ion.[19,51] It can be seen that the sputter yield of ice using C_{60}^+ ion beam was significantly higher than that of Au_3^+ and Ar_{1800}^+ ion beams with the same kinetic energy. The lower sputtering yield observed for Au_3 than for C_{60} projectiles can be attributed to a difference in the shape of profiles of deposited energy. Because the Au_3^+ trimer was much smaller than the C_{60}^+ cluster, the interaction of Au_3^+ projectile with ice was weaker, and it deposited its kinetic energy over a much longer distance compared to the C_{60}^+ projectile.[19,51,65] Therefore, a Au_3^+ projectile deposited a smaller density of energy near the surface of sample and thus exhibited a lower sputter yield. However, the energy deposition depth for C_{60}^+ and Ar_{1800}^+ clusters is comparable, and the occurrence of such a significant difference in measured sputter yields between these two projectiles is puzzling.

Computer simulations were employed to resolve this mystery. The calculated sputtering yields for a 20 keV C_{60} and Ar_{1800} impacts at 45° are approximately 2280 and 1400 water molecule equivalents, respectively. These values agree with the experimental data. The simulations show that molecules are emitted by different processes when the ice sample is bombarded by C_{60} and Ar_{1800} clusters (see Videos S1 and S2). The C_{60} projectile transfers most of its energy into the sample. It creates a hot volume where ice sublimates abruptly into molecular gas. The gas bubble expands, pushing surrounding materials. The molecules are ejected by a fluid flow motion of material along the walls of the forming crater, followed by effusion of molecules from within the crater. Such a behavior is typical for medium-size cluster bombardment.[66] A formation of a spherical crater with a relatively symmetrical rim, as shown in Figure 3a, is a consequence of this process. Most of the material is sputtered in the form of separate water molecules or small water clusters. The scenario leading to material ejection stimulated by the Ar_{1800} impact is different. In this case, the material is removed from the sample predominantly by the washing-out mechanism for off-normal impacts.[66] Initially, the projectile compresses the ice and then deforms. It acts like a liquid droplet. An intense flux of Ar atoms "sliding" over the bottom and right side of the crater is formed. Subsequently, this flux blocks the effusion of molecules from the walls of the forming crater. The interaction of sliding Ar atoms with weakly bound water molecules leads to the ejection of these particles.

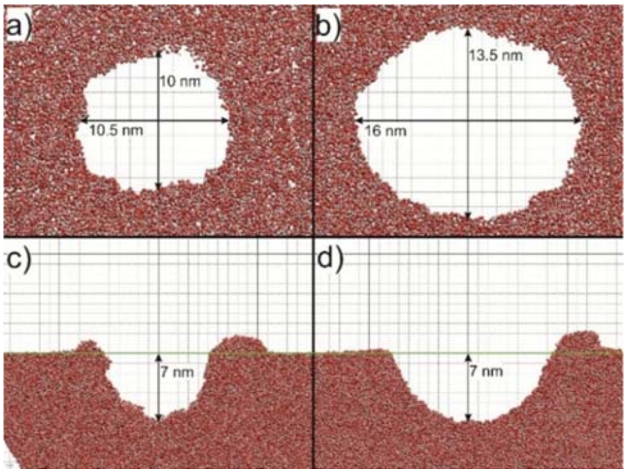

Figure 3. Craters formed by 20 keV C_{60} (panels a,c) and Ar_{1800} (panels b,d) projectiles impacting at 45° on the ice sample. The top row shows a 1 nm-thick slice on the top of sample. The bottom row shows a 2 nm-thick cut through the sample centered at the point of projectile impact. The green line in the bottom row depicts the level of the sample surface. Thin and thick lines in the background are separated by 1 and 10 nm in distance, respectively.

Impacts of both C_{60} and Ar_{1800} projectiles lead to the formation of craters. It is surprising, however, that the crater formed by the C_{60} impact is smaller, as presented in Figure 3, despite the fact that this projectile has the largest sputtering yield. Both craters have a similar depth of 7 nm. The crater formed by the C_{60} impact is symmetric with a circular cross-section at the surface of the sample. The Ar_{1800} crater is elliptical at the surface level and elongated in the direction of the impact azimuth. It is larger than the C_{60} crater. The difference in the mass displacement caused by the impacts of these two projectiles is responsible for this apparent contradiction. This displacement is more significant for larger and more massive Ar clusters. Part of the relocated material is ejected while the remaining part accumulates in the rim around the crater, as shown in Figure 4. It is evident that the Ar_{1800} impact creates much broader and taller rim than C_{60}.

3D Molecular Imaging of Frozen Milk. 3D molecular imaging of frozen homogenized milk was conducted to further demonstrate the potential of *in situ* liquid SIMS. Figure 5 shows pseudo-3D reconstruction results of four selected positive ions of the milk sample, namely, Si^+, Na^+, positive

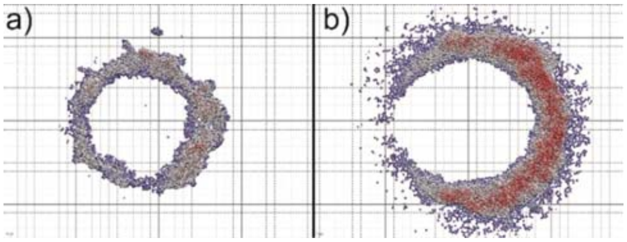

Figure 4. Rims of craters formed by impacts of (a) 20 keV C_{60} and (b) 20 keV Ar_{1800} projectiles at 45° on the ice sample. Colors depict the height of rim, with blue at its base and red at the height of 2.5 nm and above. Thin and thick lines in the background are separated by 1 and 10 nm in distance, respectively.

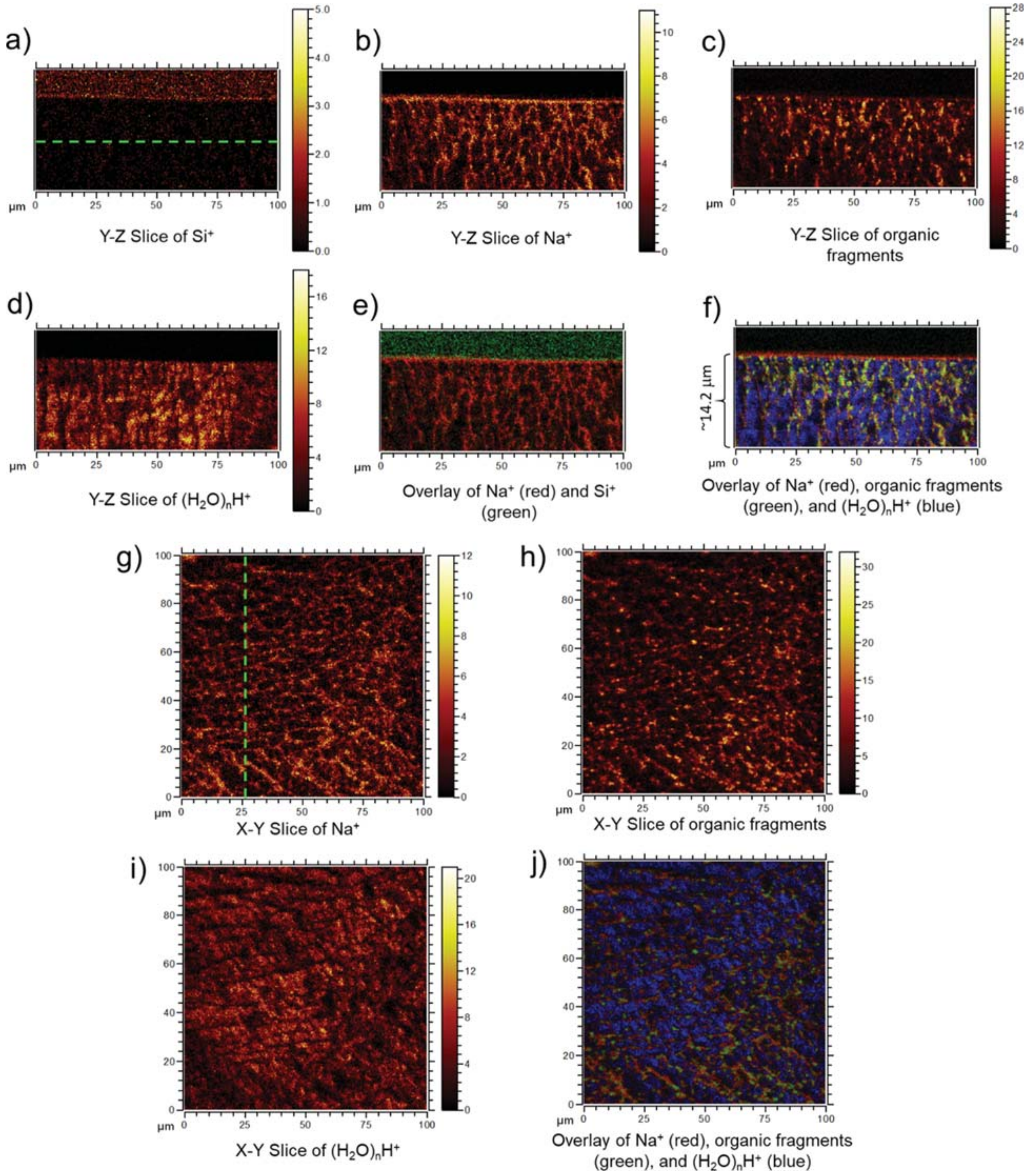

Figure 5. Positive-ion images showing pseudo-3D reconstruction results of selected species in a frozen milk sample. (a−f) Are *Y*−*Z* slices to show depth distributions of selected ion species at an arbitrarily chosen cross-section location, corresponding to the plane in an *X*−*Y* slice denoted by a green dashed line in (g). (g−j) Are *X*−*Y* slices, with a size of 100 × 100 μm^2, to show horizontal distributions of selected ion species at an arbitrarily chosen depth, corresponding to a plane in a *Y*−*Z* slice denoted by a green dashed line in (a). Si^+ (a) was shown to represent the SiN membrane. Na^+ (b,g) was a typical inorganic ion in milk. Organic species (c,h) included CH_3^+, $C_2H_3^+$, $C_2H_5^+$, CH_4N^+, OCH_3^+, $C_3H_7^+$, $C_2H_6N^+$, $C_4H_3^+$, $C_4H_5^+$, $C_5H_7^+$, $C_5H_9^+$, $C_6H_5^+$, $C_6H_9^+$, and $C_6H_{11}^+$. Water clusters (d,i), including $(H_2O)_{5-10}H^+$, were used to represent ice in the frozen milk. The thickness of the milk in (a−f) was ca. 14.2 μm [as shown in (f)], which was estimated based on the sputter rate of pure ice.

organic fragments (e.g., $C_xH_y^+$), and water clusters [$(H_2O)_nH^+$]. Among these ions, Si^+ originated from the SiN window of the microdevice while the other three ions originated from the milk sample. The thickness of the milk was estimated as 14.2 μm, assuming that the sputter yield of milk was comparable to that of ice. The distributions of these four ions across a *Y*−*Z* plane are shown in Figure 5a−f while the distributions across an *X*−*Y* plane are shown in Figure 5g−

j. A clear boundary between the SiN and the milk sample was observed along the *Z*-direction, indicating the good confinement of the milk sample within the chamber. For ions originating from the milk sample, one interesting observation was that higher signal intensity of Na^+ was found near the interface between SiN and the sample, suggesting a layer of concentrated Na^+ at the interface (Figure 5b,e,f). Such a concentrated layer was absent for both organic fragments and water clusters (Figure 5c−f). Meanwhile, comparing Figure 5c,d,f revealed a reverse distribution of organic fragments and water clusters. Surprisingly, it was noticed that the spatial distribution of Na^+ aligned better with that of organic fragments, implying that despite its high hydrophilicity, Na^+ in homogenized milk was better associated with organic matters rather than water components. Similar trends of spatial distribution of Na^+, organic fragments, and water clusters were also observed in images constructed on an *X*−*Y* plane (Figure 5g−j). Furthermore, it was found that the distribution of both Na^+ and organic fragments exhibited a porous network structure with a pore size of 3−4 μm, which matched well with protein networks observed in cryo-SEM imaging.[67] In addition, "hot spots" were observed in the image for organic fragments, and a comparison with previously reported cryo-SEM and confocal laser scanning microscopy (CLSM) results indicated that they were highly possibly related to fatty acids in fat globules.[67]

Figure S3 shows imaging results of four selected negative ions, namely Si^-, CN^-, fatty acid species ($C_xH_yO_2^-$), and water clusters [$(H_2O)_2OH^-$]. Among these negative ions, Si^- originated from SiN while CN^-, fatty acid species, and water clusters were fragmented from proteins, fatty acids, and water components from the milk sample, respectively. Similar to the case of positive ions, a clear boundary was observed between SiN and the sample region along the *Z*-direction. Meanwhile, a concentrated layer of CN^- was observed at the SiN/sample interface, which can be explained by the adsorption of proteins on the surface of SiN.[68,69] It was noticed that the distribution of CN^- matched well with that of Na^+, which strongly suggests that Na^+ was captured and confined by protein components in homogenized milk. More interestingly, images of organic matters (CN^- and fatty acid species) on both *Y*−*Z* and *X*−*Y* slices revealed that the microstructure of a milk sample can be separated into two regions. In the first region, similar to the one observed for positive organic species (Figure 5), both CN^- and fatty acid species exhibited a porous network with a pore size of 3−4 μm, indicating the presence of a network structure consisting of proteins and fatty acids in homogenized milk.[67] Particularly, fatty acid species (Figure S3c,h) showed more distinguishable "hot spots" compared with CN^- (Figure S3b,g), which further confirmed that the "hot spots" observed in the image of positive organic fragments (Figure 5c,h) should also originate from fatty acids. In contrast, in the second region, while hot spots were still observed for fatty acid species, a well-defined network of proteins (CN^-) was absent. Instead, CN^- exhibited a homogeneous distribution. Such a region was not observed in imaging results of positive ions. The exact reason behind different organic species distributions between positive-ion and negative-ion imaging was unknown, but current results indicate that 3D structural differences in biological samples can be easily distinguished with submicron lateral resolution using our innovation.

Taken together, the porous network structure of proteins and the fatty acids observed in a frozen homogenized milk sample using *in situ* liquid SIMS matched well with imaging results obtained using cryo-SEM.[67] Meanwhile, additional advantages of using *in situ* liquid SIMS for 3D molecular imaging can be identified. Cryo-SEM is powerful in providing structural information of biological samples, and elemental information can also be available when the cryo-SEM is used in conjugation with energy-dispersive X-ray spectroscopy or electron energy loss spectroscopy.[70] However, coating biological samples with noble metals (to reduce charging effect) is always required, and molecular details of sample constituents are difficult to obtain. In contrast, our *in situ* liquid SIMS not only provides structural information for targeting biological samples without extensive sample pretreatment but also simultaneously provides elemental and molecular information for the sample. For instance, we observed that Na^+ and protein components exhibited the same spatial distribution, which strongly suggested the binding of Na^+ by proteins in homogenized milk. Such information is inaccessible in measurements based solely on electron microscopy. On the other hand, fluorescence microscopy, such as CLSM and structured illumination microscopy (SIM), has also been widely used to perform 3D molecular imaging of biological samples.[3,71] However, in these techniques, the labeling of targeting molecules with bulky fluorophore is inevitable, which may not only impact the original behavior of biological components being labeled but also limit the number of molecules to be imaged simultaneously. In contrast, *in situ* liquid SIMS allowed for the simultaneous detection of multiple molecular fragments without further modification of targeting molecules. For instance, in this study, inorganic salts, organic species, and water clusters of a frozen milk sample were imaged at the same time, revealing the interesting reverse distribution of water component and organic species and the correlation between Na^+ and protein components. Consequently, this study demonstrated the great potential of *in situ* liquid SIMS for providing facile 3D molecular imaging of biological samples.

Depth Calibration in 3D Reconstruction. It is well known that different components may show different sputter rates, which may lead to complex image distortion in 3D SIMS image reconstruction. Ex situ scanning probe microscopy (SPM) measurement before and after SIMS testing has been used to address this issue, and such an approach can accurately calibrate depth pixel-by-pixel.[72] Unfortunately, such a method was not practical in this research because challenging environmental control (low temperature and desirable moisture) was necessary during sample transfer and SPM measurement to avoid potential ice melting, sublimation, or desublimation. In recent years, in situ SPM measurement and in situ focused ion beam SIMS have been developed.[73,74] However, such capabilities are not widely available. Therefore, in this work, the sputter rate of ice was directly used for the depth calibration of the homogenized milk samples. This approximation was reasonable based on following reasons. First, the major component of milk is water (87+ wt %). Meanwhile, lactose is a major organic component in milk (about 5 wt %). Although the sputter rate of lactose is not available, the sputter rate of a similar compound, trehalose, has been reported,[18] which was similar to the sputter rate of ice estimated in this work (both are ca. 50−60 nm^3 per 20 keV Ar cluster ion). More importantly, if the sputter rate of a component is significantly lower than ice, it will show a long tail in *Z*-direction. On the other hand, if the sputter rate of a component is significantly higher than ice, it will be more compressed in the Z-direction. However, in our SIMS images (Figures 5 and S3), both situations were not observed, and the 3D structure of milk in SIMS images was very similar with results from the previous cryo-SEM studies of milk.

Potential Applications. In recent years, the desire to develop antibacteria strategies and bioprocesses utilizing biofilms have driven ascending research efforts.[75,76] Analyzing biofilms with 3D molecular imaging has attracted particular interest because it can provide deeper mechanical insights into properties and behaviors of biofilms on the molecular level.[1,6,77] Cryogenic fixation is a widely adopted strategy to make biological samples including biofilms compatible with the high vacuum used in most of 3D imaging techniques.[22−25] However, the commonly used freezing-drying and freezing-fracturing methods suffered from either the unpredictable sample displacement or the poorly reproducible generation of fracture plane, which made them unsuitable for preparing samples of biofilms for 3D imaging. In contrast, *in situ* liquid SIMS offers unprecedented opportunities to prepare samples of biofilms for molecular imaging by allowing biofilms to directly grow on substrates inside its liquid chamber.[42] Indeed, our *in situ* liquid SIMS has already been successfully applied to study the growth of live biofilms and their extracellular polymeric substances on a liquid−solid interface with molecular details. We achieved the analysis of the response of *Shewanella oneidensis* MR-1 biofilms toward changes in environmental conditions, and water clusters in living biofilms were detected for the first time.[45,48] However, because of the fluidity of these liquid samples, previous chemical mappings of biofilms using *in situ* liquid SIMS were only gained in limited field-of-view (about 2 μm in diameter with nanoscale depth). Our current study demonstrates that such limitations can be overcome by implementing the flash-freezing technique into *in situ* liquid SIMS. Using this method, biofilms grown in the liquid chamber can be "locked" in a designated *in situ* status with high reproducibility, and molecular imaging with 3D resolution can be acquired for the solid sample there formed.

Recently, it has been reported that the flash-frozen cells can be directly analyzed using the SIMS instrument without drying or fracturing. For example, Winograd and Benkovic et al. used this sample preparation method and SIMS imaging to visualize purine biosynthesis by purinosome, providing direct molecular evidence to confirm a long-time hypothesis in understanding of metabolic pathway.[7] This is a beautiful development over traditional freeze-drying and freeze-fracturing methods. Compared to this method, a major advantage of our new development is the convenience of *in situ* examination of complex chemistries occurring at the solid−liquid interface, such as biofilm attachment/detachment.

The potential of our new development for 3D molecular imaging can be further extended to a much wider range of samples. For instance, various emulsions have been recognized as crucial parts in the fields of food science and wastewater treatment.[78−81] 3D molecular imaging on these emulsions can be advantageous in revealing their hierarchical structures and the presence of any potential surfactant effect, which can further advance understanding in the related fields.[78−81]

CONCLUSIONS

In this work, we used ice and frozen milk as examples to demonstrate the capability of our improved *in situ* liquid SIMS device for 3D molecular imaging of biological samples. The unique advantage of our innovation is the convenient and highly controllable sample preparation, which enables the precise design on the cell depth and thus the easy determination of sputter yields of ice. For the first time, sputter yield of a 20 keV Ar_{1800}^+ ion on ice has been experimentally determined as 1500 (±8%) water molecules per 20 keV Ar_{1800}^+ ion, which matched well with the results from MD simulations. Furthermore, molecular imaging of a frozen milk sample was acquired using our innovation to demonstrate its compatibility with biological samples. The imaging results on Na^+, water clusters, and organic fragments clearly revealed a reverse distribution of water components and organic species. A porous network structure majorly consisting of proteins was observed, and Na^+ appeared to accompany with proteins rather than water components. Meanwhile, fatty acids were found to form droplets and attach on the protein network. Our 3D imaging observation of the frozen milk sample was in accordance with cryo-SEM imaging results previously reported. We anticipate that our innovation will offer great opportunities to gain a deeper insight into biological structures and their behaviors, as well as many other liquid systems. For example, biofilm attachment/detachment and 3D structure of emulsions will be examined in our future research.

ASSOCIATED CONTENT

Supporting Information

The Supporting Information is available free of charge at https://pubs.acs.org/doi/10.1021/acs.analchem.0c02204.

Calculation details of sputter rate of ice, more experimental details, the reproducibility of SIMS measurement, and negative-ion images of the milk sample (PDF)

Emission of molecules by different processes when the ice sample is bombarded by C60_side_cut (MP4)

Emission of molecules by different processes when the ice sample is bombarded by Ar1800_side_cut (MP4)

AUTHOR INFORMATION

Corresponding Authors

Zihua Zhu − *Environmental Molecular Sciences Laboratory, Pacific Northwest National Laboratory, Richland, Washington 99354, United States;* orcid.org/0000-0001-5770-8462; Email: zihua.zhu@pnnl.gov

Wei David Wei − *Department of Chemistry and Center for Catalysis, University of Florida, Gainesville, Florida 32611, United States;* orcid.org/0000-0002-3121-5798; Email: wei@chem.ufl.edu

Zbigniew Postawa − *Smoluchowski Institute of Physics, Jagiellonian University, Kraków 31-007, Poland;* orcid.org/0000-0002-7643-5911; Email: zbigniew.postawa@uj.edu.pl

Authors

Wenxiao Guo − *Environmental Molecular Sciences Laboratory, Pacific Northwest National Laboratory, Richland, Washington 99354, United States; Department of Chemistry and Center for Catalysis, University of Florida, Gainesville, Florida 32611, United States;* orcid.org/0000-0002-6674-9714

Michal Kanski − *Smoluchowski Institute of Physics, Jagiellonian University, Kraków 31-007, Poland*

Wen Liu − *Environmental Molecular Sciences Laboratory, Pacific Northwest National Laboratory, Richland, Washington 99354, United States*

Mikołaj Gołuński − *Smoluchowski Institute of Physics, Jagiellonian University, Kraków 31-007, Poland*
Yadong Zhou − *Environmental Molecular Sciences Laboratory, Pacific Northwest National Laboratory, Richland, Washington 99354, United States*
Yining Wang − *Physical and Computational Sciences Directorate, Pacific Northwest National Laboratory, Richland, Washington 99354, United States*
Cuixia Cheng − *Environmental Molecular Sciences Laboratory, Pacific Northwest National Laboratory, Richland, Washington 99354, United States*
Yingge Du − *Physical and Computational Sciences Directorate, Pacific Northwest National Laboratory, Richland, Washington 99354, United States;* orcid.org/0000-0001-9680-1950

Complete contact information is available at:
https://pubs.acs.org/10.1021/acs.analchem.0c02204

Notes

The authors declare no competing financial interest.

■ ACKNOWLEDGMENTS

This work was supported by LDRD programs (FY2016 open call and partially Chemical Dynamics Initiative) of the Pacific Northwest National Laboratory (PNNL). The device was designed by Z.Z. with some help from Y.D. SIMS measurement was performed at EMSL, a national scientific user facility sponsored by the Department of Energy's Office of Biological and Environmental Research located at PNNL. MD simulations were performed at the PLGrid Infrastructure. Z.P. would like to acknowledge support from the Polish National Science Center Program no. 2019/33/B/ST4/01778. W.D.W. and W.G. especially appreciate support of a graduate school fellowship from the University of Florida. W.G. was also partially supported by the U.S. Department of Energy, Office of Science, Office of Workforce Development for Teachers and Scientists, and Office of Science Graduate Student Research (SCGSR) program. The SCGSR program is administered by the Oak Ridge Institute for science and Education for the DOE under contract number DE-SC0014664.

■ REFERENCES

(1) Kompauer, M.; Heiles, S.; Spengler, B. *Nat. Methods* **2017**, *14*, 1156−1158.

(2) Neumann, E. K.; Do, T. D.; Comi, T. J.; Sweedler, J. V. *Angew. Chem., Int. Ed.* **2019**, *58*, 9348.

(3) Wu, Y.; Shroff, H. *Nat. Methods* **2018**, *15*, 1011−1019.

(4) De Niz, M.; Burda, P.-C.; Kaiser, G.; Del Portillo, H. A.; Spielmann, T.; Frischknecht, F.; Heussler, V. T. *Nat. Rev. Microbiol.* **2017**, *15*, 37−54.

(5) Zhang, L.; Vertes, A. *Angew. Chem., Int. Ed.* **2018**, *57*, 4466−4477.

(6) Sigal, Y. M.; Zhou, R.; Zhuang, X. *Science* **2018**, *361*, 880.

(7) Pareek, V.; Tian, H.; Winograd, N.; Benkovic, S. J. *Science* **2020**, *368*, 283.

(8) Jung, S.; Foston, M.; Kalluri, U. C.; Tuskan, G. A.; Ragauskas, A. J. *Angew. Chem., Int. Ed.* **2012**, *51*, 12005−12008.

(9) Seeley, E. H.; Caprioli, R. M. *Anal. Chem.* **2012**, *84*, 2105−2110.

(10) Passarelli, M. K.; Pirkl, A.; Moellers, R.; Grinfeld, D.; Kollmer, F.; Havelund, R.; Newman, C. F.; Marshall, P. S.; Arlinghaus, H.; Alexander, M. R.; West, A.; Horning, S.; Niehuis, E.; Makarov, A.; Dollery, C. T.; Gilmore, I. S. *Nat. Methods* **2017**, *14*, 1175.

(11) Fletcher, J. S.; Vickerman, J. C. *Anal. Chem.* **2013**, *85*, 610−639.

(12) Tian, H.; Sparvero, L. J.; Blenkinsopp, P.; Amoscato, A. A.; Watkins, S. C.; Bayır, H.; Kagan, V. E.; Winograd, N. *Angew. Chem., Int. Ed.* **2019**, *58*, 3156−3161.

(13) Fletcher, J. S.; Lockyer, N. P.; Vaidyanathan, S.; Vickerman, J. C. *Anal. Chem.* **2007**, *79*, 2199−2206.

(14) Brison, J.; Robinson, M. A.; Benoit, D. S. W.; Muramoto, S.; Stayton, P. S.; Castner, D. G. *Anal. Chem.* **2013**, *85*, 10869−10877.

(15) Bailey, J.; Havelund, R.; Shard, A. G.; Gilmore, I. S.; Alexander, M. R.; Sharp, J. S.; Scurr, D. J. *ACS Appl. Mater. Interfaces* **2015**, *7*, 2654−2659.

(16) Winograd, N. *Annu. Rev. Anal. Chem.* **2018**, *11*, 29−48.

(17) Winograd, N. *Anal. Chem.* **2005**, *77*, 142 A−149 A.

(18) Shen, K.; Wucher, A.; Winograd, N. *J. Phys. Chem. C* **2015**, *119*, 15316−15324.

(19) Russo, M. F.; Szakal, C.; Kozole, J.; Winograd, N.; Garrison, B. J. *Anal. Chem.* **2007**, *79*, 4493−4498.

(20) Tian, H.; Six, D. A.; Krucker, T.; Leeds, J. A.; Winograd, N. *Anal. Chem.* **2017**, *89*, 5050−5057.

(21) Rabbani, S.; Barber, A. M.; Fletcher, J. S.; Lockyer, N. P.; Vickerman, J. C. *Anal. Chem.* **2011**, *83*, 3793−3800.

(22) Schaepe, K.; Kokesch-Himmelreich, J.; Rohnke, M.; Wagner, A.-S.; Schaaf, T.; Wenisch, S.; Janek, J. *Biointerphases* **2015**, *10*, 019016.

(23) Malm, J.; Giannaras, D.; Riehle, M. O.; Gadegaard, N.; Sjövall, P. *Anal. Chem.* **2009**, *81*, 7197−7205.

(24) Cannon, D. M.; Pacholski, M. L.; Winograd, N.; Ewing, A. G. *J. Am. Chem. Soc.* **2000**, *122*, 603−610.

(25) Winograd, N.; Bloom, A. *Methods Mol. Biol.* **2015**, *1203*, 9−19.

(26) Gulin, A.; Nadtochenko, V.; Astafiev, A.; Pogorelova, V.; Rtimi, S.; Pogorelov, A. *Analyst* **2016**, *141*, 4121−4129.

(27) Lanekoff, I.; Phan, N. T.; Van Bell, C. T.; Winograd, N.; Sjövall, P.; Ewing, A. G. *Surf. Interface Anal.* **2013**, *45*, 211−214.

(28) Passarelli, M. K.; Newman, C. F.; Marshall, P. S.; West, A.; Gilmore, I. S.; Bunch, J.; Alexander, M. R.; Dollery, C. T. *Anal. Chem.* **2015**, *87*, 6696−6702.

(29) Newman, C. F.; Havelund, R.; Passarelli, M. K.; Marshall, P. S.; Francis, I.; West, A.; Alexander, M. R.; Gilmore, I. S.; Dollery, C. T. *Anal. Chem.* **2017**, *89*, 11944−11953.

(30) Mohammadi, A. S.; Li, X.; Ewing, A. G. *Anal. Chem.* **2018**, *90*, 8509−8516.

(31) Johansson, B. *Surf. Interface Anal.* **2006**, *38*, 1401−1412.

(32) Rabbani, S.; Fletcher, J. S.; Lockyer, N. P.; Vickerman, J. C. *Surf. Interface Anal.* **2011**, *43*, 380−384.

(33) Lanekoff, I.; Kurczy, M. E.; Adams, K. L.; Malm, J.; Karlsson, R.; Sjövall, P.; Ewing, A. G. *Surf. Interface Anal.* **2011**, *43*, 257−260.

(34) Ostrowski, S. G.; Van Bell, C. T.; Winograd, N.; Ewing, A. G. *Science* **2004**, *305*, 71.

(35) Kurczy, M. E.; Piehowski, P. D.; Van Bell, C. T.; Heien, M. L.; Winograd, N.; Ewing, A. G. *Proc. Natl. Acad. Sci. U.S.A.* **2010**, *107*, 2751−2756.

(36) Lanekoff, I.; Sjövall, P.; Ewing, A. G. *Anal. Chem.* **2011**, *83*, 5337−5343.

(37) Fletcher, J. S.; Rabbani, S.; Henderson, A.; Lockyer, N. P.; Vickerman, J. C. *Rapid Commun. Mass Spectrom.* **2011**, *25*, 925−932.

(38) Piwowar, A. M.; Keskin, S.; Delgado, M. O.; Shen, K.; Hue, J. J.; Lanekoff, I.; Ewing, A. G.; Winograd, N. *Surf. Interface Anal.* **2013**, *45*, 302−304.

(39) Piwowar, A. M.; Fletcher, J. S.; Kordys, J.; Lockyer, N. P.; Winograd, N.; Vickerman, J. C. *Anal. Chem.* **2010**, *82*, 8291−8299.

(40) Roddy, T. P.; Cannon, D. M.; Ostrowski, S. G.; Ewing, A. G.; Winograd, N. *Anal. Chem.* **2003**, *75*, 4087−4094.

(41) Yang, L.; Yu, X.-Y.; Zhu, Z.; Iedema, M. J.; Cowin, J. P. *Lab Chip* **2011**, *11*, 2481−24844.

(42) Hua, X.; Yu, X.-Y.; Wang, Z.; Yang, L.; Liu, B.; Zhu, Z.; Tucker, A. E.; Chrisler, W. B.; Hill, E. A.; Thevuthasan, T.; Lin, Y.; Liu, S.; Marshall, M. J. *Analyst* **2014**, *139*, 1609−1613.

(43) Zhu, Z.; Zhou, Y.; Yan, P.; Vemuri, R. S.; Xu, W.; Zhao, R.; Wang, X.; Thevuthasan, S.; Baer, D. R.; Wang, C.-M. *Nano Lett.* **2015**, *15*, 6170−6176.

(44) Yu, J.; Zhou, Y.; Hua, X.; Liu, S.; Zhu, Z.; Yu, X.-Y. *Chem. Commun.* **2016**, *52*, 10952−10955.

(45) Ding, Y.; Zhou, Y.; Yao, J.; Szymanski, C.; Fredrickson, J.; Shi, L.; Cao, B.; Zhu, Z.; Yu, X.-Y. *Anal. Chem.* **2016**, *88*, 11244−11252.

(46) Zhang, Y.; Su, M.; Yu, X.; Zhou, Y.; Wang, J.; Cao, R.; Xu, W.; Wang, C.; Baer, D. R.; Borodin, O.; Xu, K.; Wang, Y.; Wang, X.-L.; Xu, Z.; Wang, F.; Zhu, Z. *Anal. Chem.* **2018**, *90*, 3341−3348.

(47) Zhang, Y.; Wang, J.-G.; Yu, X.; Baer, D. R.; Zhao, Y.; Mao, L.; Wang, F.; Zhu, Z. *ACS Energy Lett.* **2019**, *4*, 215−221.

(48) Ding, Y.; Zhou, Y.; Yao, J.; Xiong, Y.; Zhu, Z.; Yu, X.-Y. *Analyst* **2019**, *144*, 2498−2503.

(49) Zhang, Y.; Zeng, W.; Huang, L.; Liu, W.; Jia, E.; Zhao, Y.; Wang, F.; Zhu, Z. *Anal. Chem.* **2019**, *91*, 7039−7046.

(50) Breitenstein, D.; Rommel, C. E.; Möllers, R.; Wegener, J.; Hagenhoff, B. *Angew. Chem., Int. Ed.* **2007**, *46*, 5332−5335.

(51) Szakal, C.; Kozole, J.; Winograd, N. *Appl. Surf. Sci.* **2006**, *252*, 6526−6528.

(52) Taylor, A. J.; Graham, D. J.; Castner, D. G. *Analyst* **2015**, *140*, 6005−6014.

(53) Wucher, A.; Cheng, J.; Zheng, L.; Winograd, N. *Anal. Bioanal. Chem.* **2009**, *393*, 1835−1842.

(54) Adrian, M.; Dubochet, J.; Lepault, J.; McDowall, A. W. *Nature* **1984**, *308*, 32−36.

(55) Zhou, Y.; Yao, J.; Ding, Y.; Yu, J.; Hua, X.; Evans, J. E.; Yu, X.; Lao, D. B.; Heldebrant, D. J.; Nune, S. K.; Cao, B.; Bowden, M. E.; Yu, X.-Y.; Wang, X.-L.; Zhu, Z. *J. Am. Soc. Mass Spectrom.* **2016**, *27*, 2006−2013.

(56) Garrison, B. J.; Postawa, Z. Molecular dynamics simulations, the theoretical partner to dynamic cluster SIMS experiments. In *ToF-SIMS—Surface Analysis by Mass Spectrometry*, 2nd ed; Briggs, D.; Vickerman, J. C., Eds.; SurfaceSpectra Ltd./IM Publications, 2013.

(57) Aziz, R. A.; Slaman, M. J. *Mol. Phys.* **1986**, *58*, 679−697.

(58) Wilson, W. D.; Haggmark, L. G.; Biersack, J. P. *Phys. Rev. B* **1977**, *15*, 2458−2468.

(59) Zhang, W.; van Duin, A. C. T. *J. Phys. Chem. B* **2017**, *121*, 6021−6032.

(60) Ziegler, J. F.; Biersack, J. P. The Stopping and range of ions in matter. In *Treatise on Heavy-Ion Science*; Bromley, D. A., Ed.; Astrophysics, Chemistry, and Condensed Matter; Springer US, 1985; Vol. *6*, pp 93−129.

(61) Postawa, Z.; Czerwinski, B.; Szewczyk, M.; Smiley, E. J.; Winograd, N.; Garrison, B. J. *Anal. Chem.* **2003**, *75*, 4402−4407.

(62) Plimpton, S. *J. Comput. Phys.* **1995**, *117*, 1−19.

(63) Castellanos, A.; Ramirez, C. E.; Michalkova, V.; Nouzova, M.; Noriega, F. G.; Fernández-Lima, F. *J. Anal. At. Spectrom.* **2019**, *34*, 874−883.

(64) Fletcher, J. S.; Lockyer, N. P.; Vickerman, J. C. *Mass Spectrom. Rev.* **2011**, *30*, 142−174.

(65) Russo, M. F.; Wojciechowski, I. A.; Garrison, B. J. *Appl. Surf. Sci.* **2006**, *252*, 6423−6425.

(66) Czerwinski, B.; Rzeznik, L.; Paruch, R.; Garrison, B. J.; Postawa, Z. *Nucl. Instrum. Methods Phys. Res. Sect. B Beam Interact. Mater. Atoms* **2011**, *269*, 1578−1581.

(67) Ong, L.; Dagastine, R. R.; Kentish, S. E.; Gras, S. L. *LWT—Food Sci. Technol.* **2011**, *44*, 1291−1302.

(68) Niedzwiecki, D. J.; Grazul, J.; Movileanu, L. *J. Am. Chem. Soc.* **2010**, *132*, 10816−10822.

(69) Yu, J.; Zhou, Y.; Engelhard, M.; Zhang, Y.; Son, J.; Liu, S.; Zhu, Z.; Yu, X. Y. *Sci. Rep.* **2020**, *10*, 3695.

(70) Holling, N.; Dedi, C.; Jones, C. E.; Hawthorne, J. A.; Hanlon, G. W.; Salvage, J. P.; Patel, B. A.; Barnes, L. M.; Jones, B. V. *FEMS Microbiol. Lett.* **2014**, *355*, 20−27.

(71) Schlafer, S.; Meyer, R. L. *J. Microbiol. Methods* **2017**, *138*, 50−59.

(72) Wucher, A.; Cheng, J.; Winograd, N. *Anal. Chem.* **2007**, *79*, 5529−5539.

(73) Tiddia, M.; Mihara, I.; Seah, M. P.; Trindade, G. F.; Kollmer, F.; Roberts, C. J.; Hague, R.; Mula, G.; Gilmore, I. S.; Havelund, R. *ACS Appl. Mater. Interfaces* **2019**, *11*, 4500−4506.

(74) Spampinato, V.; Dialameh, M.; Franquet, A.; Fleischmann, C.; Conard, T.; van der Heide, P.; Vandervorst, W. *Anal. Chem.* **2020**, *92*, 11413.

(75) Liu, Y.; Shi, L.; Su, L.; van der Mei, H. C.; Jutte, P. C.; Ren, Y.; Busscher, H. J. *Chem. Soc. Rev.* **2019**, *48*, 428−446.

(76) Boudarel, H.; Mathias, J. D.; Blaysat, B.; Grediac, M. *npj Biofilms Microbiomes* **2018**, *4*, 17.

(77) Zhang, N.; Thompson, C. E. L.; Townend, I. H.; Rankin, K. E.; Paterson, D. M.; Manning, A. J. *Environ. Sci. Technol.* **2018**, *52*, 13306−13313.

(78) Ding, M.; Zhang, T.; Zhang, H.; Tao, N.; Wang, X.; Zhong, J. *Food Chem.* **2020**, *309*, 125642.

(79) Zhang, T.; Ding, M.; Zhang, H.; Tao, N.; Wang, X.; Zhong, J. *Food Chem.* **2020**, *308*, 125597.

(80) Son, J.; Shen, Y.; Yao, J.; Paynter, D.; Yu, X.-Y. *Chemosphere* **2019**, *236*, 124345.

(81) Shen, Y.; Yao, J.; Son, J.; Zhu, Z.; Yu, X.-Y. *Phys. Chem. Chem. Phys.* **2020**, *22*, 11771−11782.

https://dx.doi.org/10.1021/acs.analchem.0c02204
Anal. Chem. 2020, 92, 13785−13793